Journal of Ceramic Processing Research. Vol. 18, No. 9, pp. 666~670 (2017)

J O U R N A L O F
Ceramic Processing Research

Geometric reconstruction and numerical analysis for characterization of transport properties at various levels of water saturation in micro/nano structure of catalyst layers

Seoung-Ju Lee[a], Seong Shin[b], Jung Hun Yoo[b] and Sung-Chul Yi[a,b,*]

[a]*Department of Hydrogen and Fuel Cell Technology, Hanyang University, Haengdang-dong, Seongdong-gu, Seoul 133-791, Korea*
[b]*Department of Chemical Engineering, Hanyang University, Haengdang-dong, Seongdong-gu, Seoul 133-791, Korea*

Water transport across membrane-electrode assemblies is one of the key factors in determining the performance of proton-exchange membrane fuel cells (PEMFCs). In particular, the water saturation in the catalyst layers (CLs) is significantly related to the gas transport to the reaction sites and the ionic conductivity decided by water activity. Herein, to investigate the effect of CL structure on water transport, we compare the transport properties at various water saturation levels of two CLs, namely conventional CL and nanosized dense-structured (NSDS) CL. The two CLs were three-dimensionally reconstructed using focused ion beam-scanning electron microscopy tomography. Subsequently, the structural and transport properties were calculated based on the reconstructed CLs. The results show that the smaller pore size of the NSDS CL led to lower water permeability (a high water-retaining property) and lower saturation (water-flooding prevention). Thus, this provides insight into how the CLs could be used in the water management of PEMFCs to improve their performance.

Key words: Micro/nano structure, Catalyst layer, Water imbibition, Reconstruction, Model.

Introduction

Because of their high efficiency with low emission of pollutants, proton-exchange membrane fuel cells (PEMFCs) are being considered as a potential power generator for transportation and stationary applications. In the membrane-electrode assembly (MEA) of PEMFCs, hydrogen and oxygen pass through the porous gas diffusion layers (GDLs) and react at the catalyst layers (CLs) involving electron and ion transport to generate water and heat. Thus, the MEA should provide proper mass and charge transport properties for high cell performance. In particular, the membrane and CLs must maintain high ionic conductivity with sufficient water, but to ensure enough reactant gas transport, the GDLs and CLs should not be clogged with liquid water (water flooding) [1-2]. Generally, since the water produced at the cathode CL cannot sufficiently diffuse to the anode, the PEMFCs need external humidification of the reactants, which increases the cost and complexity of the system and is thereby impeding their commercialization [3-5]. Therefore, a number of researchers have been interested in water management to overcome the disadvantages of using external humidification. To optimize the cell design for water balance, operating conditions and gas flow-field design for the cathode have been investigated using experimental and numerical methods [6-11], but only a few researches have been focused on the anode [12-13]. Furthermore, reduced membrane thickness has been examined to facilitate the water diffusion from the cathode to the anode by increasing the water gradient across the MEA [14-15]. In addition, microporous layers have been applied to the electrodes in MEAs to control water transport by their hydrophilicity/hydrophobicity and pore structure [16-18]. Subsequently, Toyota has introduced a thin film membrane, novel flow-field structure, and internal humidification technology (counter flow configuration) to develop a PEMFC stack without a humidifier for vehicle [19].

Nevertheless, there have been attempts to improve the water-retaining property of CLs, which have enabled the preparation of a self-humidifying MEA while maintaining system simplicity. Several self-humidifying anode CLs have been designed with hygroscopic additives (e.g. SiO_2, TiO_2, etc.) to mitigate anode dehydration [20-21]. Similarly, an SiO_2 additive has been used in the cathode CLs for high cathode water concentration to enhance the back-diffusion of water from the cathode to the anode [22-24]. However, the hygroscopic additive-based CLs have mostly exhibited insufficient electrical performance due to an increase in Ohmic resistance. To address this, a dual-layered CL with hydrophilic and hydrophobic layers was implemented for the retention of produced water during low-humidity operation of PEMFCs [25]. Consequently, a dual-

*Corresponding author:
Tel : +82-2-2220-0481
Fax: +82-2-2298-5147
E-mail: scyi@hanyang.ac.kr

layered CL fabricated by introducing a phase-separated morphology via organic solvents demonstrated superior self-humidifying performance without using hygroscopic additives.

In this paper, the two CLs of the dual-layered CL [25], namely conventional CL and nanosized dense-structured (NSDS) CL, are compared in terms of the water-retaining property to gain insight into the effect of the CLs' micro/nano-structures on water transport. At first, the two CLs were three-dimensionally reconstructed using a focused ion beam (FIB)-scanning electron microscope (SEM) tomography method. Subsequently, the obtained structures served as numerical domains for calculation of the structural and transport properties of the CLs at various water saturation levels. As a result, the smaller pore size of the NSDS CL led to lower water permeability and saturation properties than those of the conventional CL. Therefore, this provides evidence that the high self-humidifying performance of the dual-layered CL arose from its tailored pore structure.

Experimental

Fabrication of the CLs

The conventional and NSDS CLs were fabricated using catalyst inks with different organic solvents to adjust the degree of phase separation which determines their structure. That is to say, 2.9 g of the 5 wt% Nafion dispersion (DE512, Ion Power) was mixed with 3.1 g of 99 wt% 1,2,3-propanetriol (Sigma Aldrich) and 99 wt% 1-methyl-2-pyrrolidinone (Sigma Aldrich) for the conventional CL and the NSDS CL, respectively. The solutions were homogenized with a vortex mixer and then sonicated after the addition of 0.1 g of 40 wt% tetrabutylammonium hydroxide (Alfa Aesar) for 1 hr at 50 °C. After that, 0.2 g of 20 wt% Pt/Carbon (HiSPEC 3000, Johnson Matthey) was added to the mixtures and they were thoroughly homogenized for 24 hrs at 50 °C. The prepared catalyst slurries were then coated on the Teflon film and dried in a convection oven at 135 and 50 °C for the conventional CL and the NSDS CL, respectively. Finally, the CLs on the Teflon films were transferred onto the Nafion membrane to form the double-layered configuration.

FIB-SEM reconstruction

In the three-dimensional (3-D) reconstruction, FIB (Helios NanoLab 600, FEI Inc.)-SEM (JSM-6300, JEOL Inc.) tomography was used to obtain actual structures of the conventional and NSDS CLs. To mitigate structural damage due to the FIB process, a thin Pt-coating was deposited onto the surfaces of the two CLs. Over a milling area of 4 × 4 μm, FIB Ga-ion milling was then conducted at 30 kV and 30 pA (in fine milling) with a cutting distance of 5 nm. At the same time for each CL, 200 slices of SEM images were taken from the cutting cross-sections at 35,000 × magnification. As shown in Fig. 1, the obtained images were stretched and rearranged to correct the angle and drift errors of the measurements. Lastly, the images were segregated into solid and pore phases by the gray-level threshold method, and then the image stacks were assembled to generate the 3-D structure of the CLs with a size of 1 × 1 × 1 μm.

Numerical analysis

To obtain the numerical domains for calculating the structural (surface area) and transport properties (capillary pressure, diffusivity, and permeability) of the CLs, the geometric modeling and analysis software Geodict 2017 was used. The domains were created with a voxel size of 5 nm and a matrix size of 200 x 200 x 200 (1 × 1 × 1 μm) for both CLs. For the 3-D

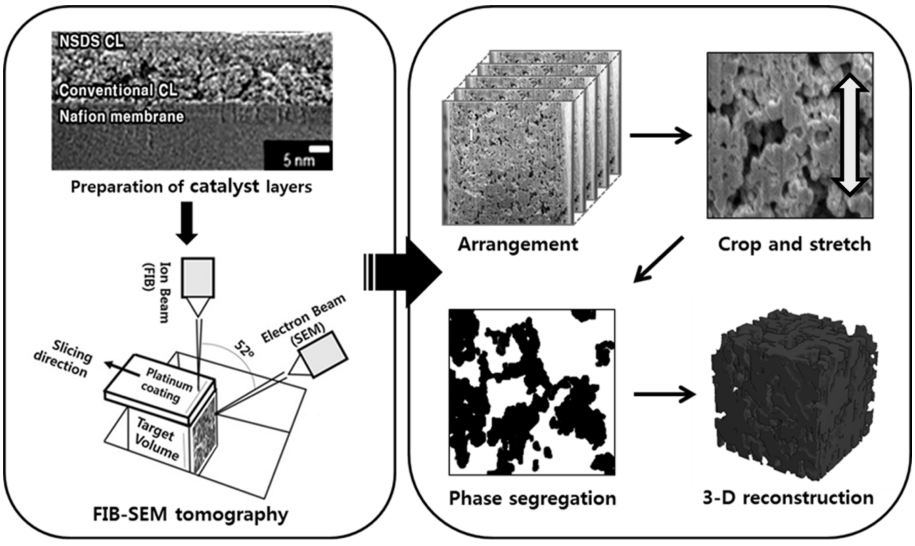

Fig. 1. 3-D reconstruction procedure of the conventional and NSDS CLs.

structures, the capillary pressure-water saturation curves were predicted with an imbibition model based on the pore morphology method [26] according to the following equation:

$$r = \frac{2\sigma}{p_c} cos\,\theta \quad (1)$$

where r is the radius of the pores, σ is the surface tension, θ is the contact angle (110 ° for conventional CL, 150 ° for NSDS CL [27]), and p_c is the capillary pressure. Subsequently, the structures with distributions of the two phases (pore and liquid water) in the CLs were used to calculate the reduction in surface area as the water saturation increased. The diffusivity dependent on the water saturation of the CLs can be estimated by the Laplace equation:

$$-(D\nabla C) = 0 \quad (2)$$

where D is the diffusivity and C is the concentration. The effective diffusivities D^{eff} can be obtained from the results of Eq. (2) with the reconstructed CLs; the tortuosity τ was evaluated by introducing D^{eff} values into the following equation:

$$\frac{D^{eff}}{D} = \frac{\varepsilon}{\tau}(1-s)^k \quad (3)$$

where ε is the porosity, s is the water saturation, and k is the saturation dependency. The effective permeability K^{eff} can be found by solving the Navier-Stokes equation with Darcy's law as follows:

$$pu \cdot \nabla u = -\nabla p + u\nabla^2 u \quad (4)$$

$$u = -\frac{K^{eff}}{u}\nabla p \quad (5)$$

where u is the velocity, μ is the viscosity, and ρ is the density.

Results and Discussion

Capillary pressure-water saturation relationship

Fig. 2(a) shows the distributions of pore and liquid water in the reconstructed structures of conventional and NSDS CLs at capillary pressure of 25, 50 and 185 (or 256) bar. When there was no liquid water, the peak pore sizes were estimated at 60 and 30 nm for the conventional (with porosity of 0.48) and NSDS (with porosity of 0.28) CLs, respectively. According to Eq. (1), the capillary pressure increases as the pore size decreases. Consequently, in the computable range, the maximum values of water saturation were found at 87.8 and 77.7% for the conventional and NSDS CLs, respectively. The capillary pressure-water saturation curves for the two CLs are illustrated in Fig. 2(b). Compared to the conventional CL, the NSDS CL had a small pore network requiring a high-pressure gradient

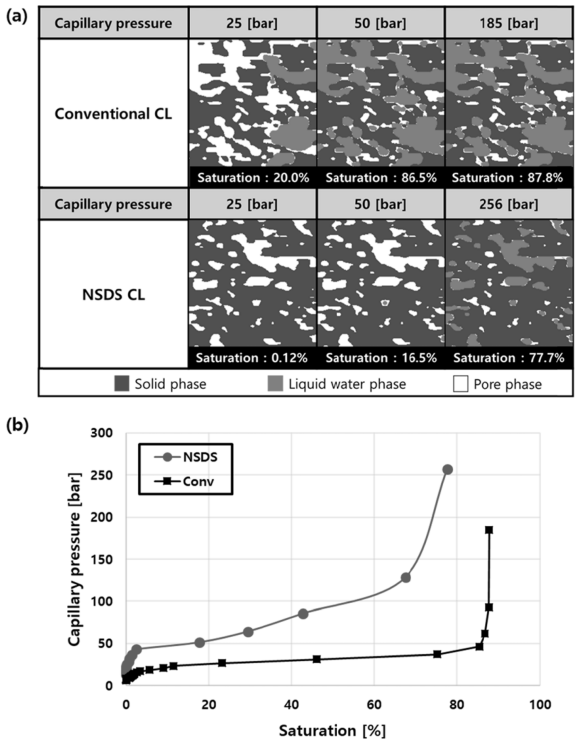

Fig. 2. Results of the water imbibition model: (a) distributions of liquid water in the two CLs, (b) capillary pressure-water saturation curves for the two CLs.

to be filled with liquid water. Thus, the NSDS CL exhibited higher capillary pressure over all of the water saturation range. In other words, at the same capillary pressure, the NSDS CL had lower water saturation than that of the conventional CL (e.g. at a capillary pressure of 25 bar, water saturation levels were 20 and 0.12% for the conventional and NSDS CLs, respectively). Therefore, when liquid water was produced, it was difficult for the water to flow through the NSDS CL due to low water saturation, which led to the disconnection of the water network.

Effects of water saturation on structural and transport properties

The structural and transport properties of CLs are dependent on the amount of liquid water in the porous structure. To obtain the properties as functions of water saturation, the reconstructed CLs with the distributions of pore and liquid water were used for the calculation. Figs. 3(a) and 3(b) shows the active surface area per volume of the CLs with respect to water saturation and capillary pressure. As expected, it can be seen that as the water saturation increased, the surface area decreased due to the pore clogging by liquid water. At a water saturation level of 0%, the conventional CL (with high porosity and large pore size) had a higher surface area than that of the NSDS CL, as shown in Fig. 3a. Hence, the surface area of the former was always higher than that of the latter regardless of water

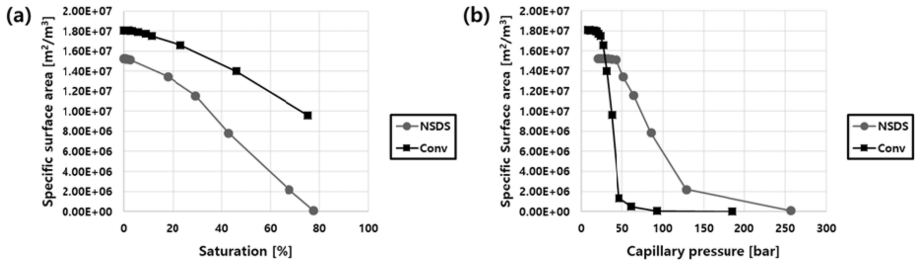

Fig. 3. Surface area of the two CLs with respect to (a) water saturation and (b) capillary pressure.

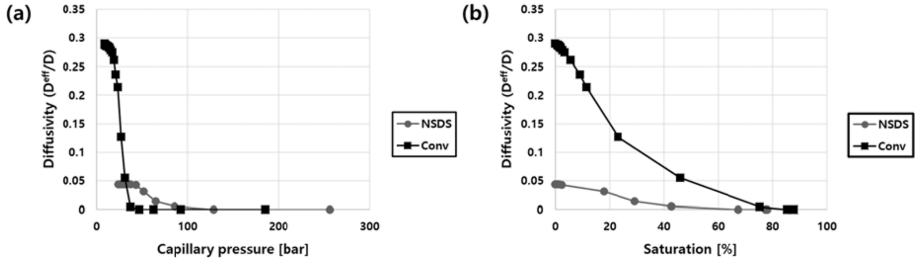

Fig. 4. Gas diffusivity in the two CLs with respect to (a) water saturation and (b) capillary pressure.

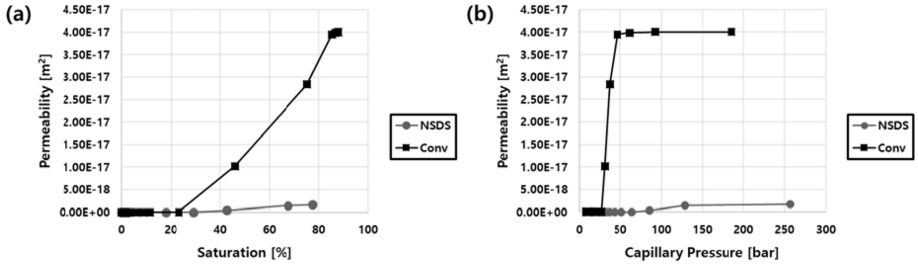

Fig. 5. Water permeability of the two CLs with respect to (a) water saturation and (b) capillary pressure.

saturation, and the difference between the surface areas of the two CLs gradually extended with increasing water saturation. However, in Fig. 3(b), the surface area of the conventional CL was dramatically reduced as the capillary pressure increased. Eventually, the NSDS CL showed a larger surface area than that of the conventional CL at a capillary pressure of more than 27 bar. This means that, compared to the conventional CL, the NSDS CL could be more advantageous in providing an active surface area for reactants under operating conditions yielding a significant amount of liquid water.

In the MEA of a PEMFC, the reactant gas transport to the reaction sites is mostly governed by diffusion. To investigate the effect of water saturation on gas diffusion, the gas diffusivities of the two CLs with respect to water saturation and capillary pressure were estimated, as shown in Figs. 4(a) and 4(b). Similar to the trend observed in the case of surface area (Fig. 3), the diffusivity decreased as more pores became filled with liquid water. According to Eq. (3), the diffusivity of the conventional CL (Fig. 4(a)) was higher than that in the NSDS CL for the range of water saturation studied due to lower tortuosity (1.8 and 6.0 for the conventional and NSDS CLs, respectively) and higher porosity (0.48). However, since the NSDS CL has low water saturation even at high capillary pressures (Fig. 2(b)), the diffusivity of the NSDS CL was higher than that of the conventional CL for capillary pressure ranging from 31 to 127 bar (Fig. 4(b)). In other words, the property of maintaining low water saturation prevented the pores clogging, thereby providing high gas diffusivity of the NSDS CL when liquid water was produced.

To discuss the difference between water transport properties of the two CLs, the liquid water permeability was analyzed at various water saturation levels and capillary pressures. As shown in Fig. 5(a), because the water flowed through the liquid phase network in the porous CLs, the water permeability is proportional to the water saturation; there is a threshold (approximately 22% water saturation) that must be exceeded for flow to occur. In addition, the NSDS CL exhibited lower water permeability than the conventional CL at the same water saturation level due to its narrow pore structure. Hence, in Fig. 5(b), because of the water saturation effect, the difference in permeability between the two CLs becomes more significant at high capillary pressure. In particular, for capillary pressure ranging from 46 to 185 bar, the water permeability of NSDS CL is less than 28

times that of the conventional CL. Therefore, it could be inferred that the water-retaining property of the NSDS CL came from its structural characteristics, which limited the formation of a water network.

Conclusions

In this paper, we report the effects of micro/nano-structure of CLs on the water-retaining property of a self-humidifying PEMFC, including investigations on the structural and transport properties dependent on the water saturation. Conventional and NSDS CLs were prepared in order to compare them using a model-based numerical analysis and were three-dimensionally reconstructed using FIB-SEM tomography to obtain their computational domains. Subsequently, the distributions of liquid water and capillary pressure-water saturation curves were estimated with the reconstructed CLs with the imbibition model. Thus, it can be seen that due to the narrow and winding pore structure, the NSDS CL had a high capillary pressure which made it difficult for water to move through it.

In addition, the surface area, gas diffusivity, and water permeability of the CLs were predicted using the reconstructed CLs with the distributions of liquid water. From the results, we confirmed that the structure of the NSDS CL was able to provide a relatively large surface area, high gas diffusivity, and low water permeability compared with the conventional CL when a significant amount of liquid water was generated. Therefore, we believe that the narrow pore structure was not only able to enhance the water-retaining property, but also played a role in improving surface area and gas diffusivity by preventing pore clogging. In conclusion, the results of this study suggest our method could be used as a guide for optimizing the performance of self-humidifying PEMFCs in terms of the micro/nano structure of the CL.

Acknowledgments

This research was supported by the Korea Electrotechnology Research Institute (KERI) and the New & Renewable Energy Core Technology Program of the Korea Institute of Energy Technology Evaluation and Planning (KETEP).

References

1. J. Chen,T. Matsuura and M. Hori, J. Power Sources 131 (2004) 155-161.
2. S. Shimpalee, U. Beuscher and J.W. Van Zee, Electrochim. Acta 52 (2007) 6748-6754.
3. G. Vasu, A.K. Tangirala, B. Viswanathan and K.S. Dhathathreyan, Int. J. Hydrogen Energy 33 (2008) 4640-4648.
4. D. Kadylak and W. Mérida, J. Power Sources 195 (2010) 3166-3175.
5. B. J. Kim and M. S. Kim, Int. J. Hydrogen Energy 37 (2012) 4290-4299.
6. J.P. Owejan, T.A. Trabold, D.L. Jacobson, M. Arif and S.G. Kandlikar, Int. J. Hydrogen Energy 32 (2007) 4489-4502.
7. S. K. Um and C.Y. Wang, J. Power Sources 156 (2006) 211-223.
8. J.W. Park, K. Jiao and X. Li, Applied Energy 87 (2010) 2180-2186.
9. H. C. Chiu, J. H. Jang, W. M. Yan, H.Y. Li and C. C. Liao, Applied Energy 96 (2012) 359-370.
10. A.K. Srouji, L.J. Zheng, R. Dross, A. Turhan and M. M. Mench, J. Power Sources 239 (2013) 433-442.
11. Z. Lu, S. G. Kandlikar, C. Rath, M. Grimm, W. Domigan, A. D. White, M. Hardbarger, J. P. Owejan and T. A. Trabold, Int. J. Hydrogen Energy 34 (2009) 3445-3456.
12. H.H. Voss, D.P. Wilkinson, P.G. Pickup, M.C. Johnson and V. Basura, Electrochim. Acta 40 (1995) 321-328.
13. S. Abbou, J. Dillet, G. Maranzana, S. Didierjean and O. Lottin, ECS Transactions 69 (2015) 1267-1276.
14. T. Susai, M. Kaneko, K. Nakato, T. Isono, A. Hamada and Y. Miyake, Int. J. Hydrogen Energy 26 (2001) 631-637.
15. G.J.M. Janseen and M.L.J. Overvelde, J. Power Sources 101 (2001) 117-125.
16. H.K. Atiyeh, K. Karan, B. Peppley, A. Phoenix, E. Halliop and J. Pharoah, J. Power Sources 170 (2007) 111-121.
17. C.J. Tseng and S.K. Lo, Energy Convers. Manage. 51 (2010) 677-684.
18. T. Kitahara, H. Nakajima, and K. Mori, J. Power Sources 199 (2012) 29-36.
19. T. Yoshida and K. Kojima, Electrochem. Soc. Interface (2015) 45-49.
20. M. Han, S.H. Chan and S.P. Jiang, Int. J. Hydrogen Energy 32 (2007) 385-391.
21. H. Su, L. Xu, H. Zhu, Y. Wu, L. Yang, S. Liao, H. Song, Z. Liang and V. Birss, Int. J. Hydrogen Energy 35 (2010) 7874-7880.
22. U. H. Jung, K. T. Park, E. H. Park and S. H. Kim, J. Power Sources 159 (2006) 529-532.
23. Z. Miao, H. Yu, W. Song, D. Zhao, L. Hao, B. Yi and Z. Shao, Electrochem. Commun. 11 (2009) 787-790.
24. N. Inoue, M. Uchida, M. Watanabe and H. Uchida, Electrochem. Commun. 16 (2012) 100-102.
25. C.Y. Jung, T.H. Kim and S.C. Yi, Chem. Sus. Chem. 7 (2014) 466-473.
26. M. Hilpert and C.T. Miller, Advances in Water Resources 24 (2001) 243-255.
27. C.Y. Jung, Z.Y. Vahc, T.H. Kim and S.C. Yi, Electrochim. Acta 146 (2014) 495-502.